Nanoscale

ROYAL SOCIETY OF CHEMISTRY

PAPER

View Article Online
View Journal | View Issue

Cite this: *Nanoscale*, 2022, **14**, 14146

In operando nanomechanical mapping of PEDOT:PSS thin films in electrolyte solutions with bimodal AFM†

Simone Benaglia, [a] Sofia Drakopoulou,[b,c] Fabio Biscarini[b,d] and Ricardo Garcia *[a]

Understanding the interplay between the nanomechanical properties of organic electronic materials and their electronic properties is central to developing sensors and transducers for applications ranging from immunosensing to e-skin. Controlling organic device operations in aqueous electrolyte solutions and their mechanical compliance with the host tissue or living systems, as for instance in active implants for the recording or stimulation of neural signals, is still largely unexplored. Here, we implemented bimodal AFM to map the nanomechanical and structural properties of thin films made from poly(3,4-ethylenedioxythiophene):poly(styrene-sulfonate) (PEDOT:PSS), the most widely used conducting polymer blend, during operation as a microelectrode in an electrolyte solution. Nanomechanical maps showed the film consisting of a granular structure made from PEDOT:PSS regions embedded in the PSS matrix. The film swelled upon immersion in an aqueous solution. *In operando* bimodal AFM data obtained by applying a sequence of doping/de-doping bias cycles showed a significant decrease in the modulus (70%) that saturated after about 10 cycles. A similar sequence of biases at the opposite polarity did not significantly influence the mechanical behaviour of PEDOT:PSS. The decrease in the modulus was explained by the development of persistent hydration, which was enhanced by the cations trapped inside the organic electronic material.

Received 20th April 2022,
Accepted 29th August 2022

DOI: 10.1039/d2nr02177c

rsc.li/nanoscale

Introduction

Organic semiconductor devices are used in a variety of applications.[1–4] Among these, organic field effect transistors are promising in biomolecular sensing and biomedicine.[4–7] In mixed ionic electronic materials, the properties of the organic materials are controlled by electrochemical doping.[4,5] Improving the performance of the devices requires an understanding of how the structure and the mechanical properties of organic semiconductors influence ion transport, and *vice versa* how ion injection modifies their electrical and structural properties.

Poly(3,4-ethylenedioxythiophene):poly(styrene-sulfonate) (PEDOT:PSS) is a widely used organic electronic material for *in vivo* active implants due to its electrochemical stability, high conductivity and biocompatibility.[8] In particular, PEDOT:PSS can be used as an active layer for organic electrochemical transistor biosensors,[9,10] neuromorphic devices,[11] and implantable devices for recording and stimulation.[12–14] In those highly dynamic conditions, the organic semiconductor might undergo a variety of nanomechanical changes that also substantially affect the electronic response.[15,16] In this context, we note that very few studies have been devoted to studying the mechanical properties of PEDOT:PSS.[17,18] To the best of our best knowledge there are no contributions that aim to address its nanoscale properties in *in operando* conditions.

Ion doping/de-doping in PEDOT:PSS thin films upon a gate electrolyte voltage bias was studied at the macroscale either by optical microscopy, for example by recording the electrochromic changes associated with the propagation of the de-doping front,[19,20] or by electrochemical quartz crystal microbalance experiments.[21] Recently some advanced atomic force microscopy (AFM) methods such as electrochemical strain,[22] photo-induced force microscopy,[23] and electrostatic force microscopy[24,25] were applied to perform *in situ* studies of the electrical properties of organic semiconductors. However,

[a]*Instituto de Ciencia de Materiales de Madrid, CSIC, c/Sor Juana Inés de la Cruz 3, 28049 Madrid, Spain. E-mail: r.garcia@csic.es*
[b]*Life Science Department, University of Modena and Reggio Emilia, Via Campi 101, 41125 Modena, Italy*
[c]*Dept. of Physics, Information Science and Mathematics, University of Modena and Reggio Emilia, Via Campi 213a, 41125 Modena, Italy*
[d]*Center for Translational Neurophysiology of Speech and Communication, Istituto Italiano di Tecnologia, Via Fossato di Mortara 17-19, Ferrara 44121, Italy*

†Electronic supplementary information (ESI) available: Description of AFM measurements and the electrical set-up, additional bimodal AFM data, force curves, and high-resolution AFM data. See DOI: **https://doi.org/10.1039/d2nr02177c**

nanoscale methods that provide real-space nanomechanical maps[26–29] have not been applied yet to study *in situ* the evolution of mechanical properties under different bias conditions. Bimodal AFM stands out among nanomechanical mapping methods because of its fast data acquisition speed, quantitative accuracy and capability of mapping at a high spatial resolution the nanomechanical properties of a large variety of materials in the liquid state.[30–33]

Here, bimodal AFM was applied to map the nanomechanical and structural properties of PEDOT:PSS thin films in air and electrolyte solution environments. We measured *in situ* the Young's modulus of PEDOT:PSS thin films in an electrolyte solution under the application of different biases. Under the application of de-doping biases (cation injection), the elastic modulus shows a significant decrease (about 70%). The overall decrease was punctuated by some small oscillations if the bias was switched to 0 V. By reversing the polarity, we observed a small increase in the elastic modulus (10%), which remained unchanged over several bias cycles. The decrease in the modulus was associated with the development of persistent hydration inside the material.

Results and discussion

Conventional AFM modes have been applied to image the morphology of PEDOT:PSS;[17,34–37] however, there were no high-spatial-resolution measurements of its nanomechanical properties. Bimodal AFM is based on the simultaneous excitation and detection of the two eigenmodes of the cantilever, commonly the first and the second modes.[38] We applied a bimodal AFM configuration that keeps the amplitude of the first mode constant to generate a topographic image (AM) while the parameters of the second mode are controlled by a frequency modulation (FM)[39] feedback (Fig. 1a). The instrument observables (first mode amplitude and phase shift and second mode frequency shift) are converted into nanomechanical properties (Young's modulus, indentation, energy dissipation) using a well-established theoretical framework detailed in the ESI.†[30,31,40–42]

High-spatial-resolution nanomechanical maps of PEDOT:PSS in air

Fig. 2 shows the topography, Young's modulus and energy dissipation maps of a region of the PEDOT:PSS film obtained in air (RH: 23%). The film exhibits a granular structure which coincides with earlier observations.[14,37] The dissipation map shows that the grains are isolated (Fig. 2b). Between the grains there is a narrow strip that provides higher values of energy dissipation. The energy dissipation signal is generated from the phase shift of the first mode (see the ESI Fig. S1†). It is established that AFM energy dissipation maps provide compositional contrast.[26,43] Thus, the observed differences between the narrow bands and the top of the

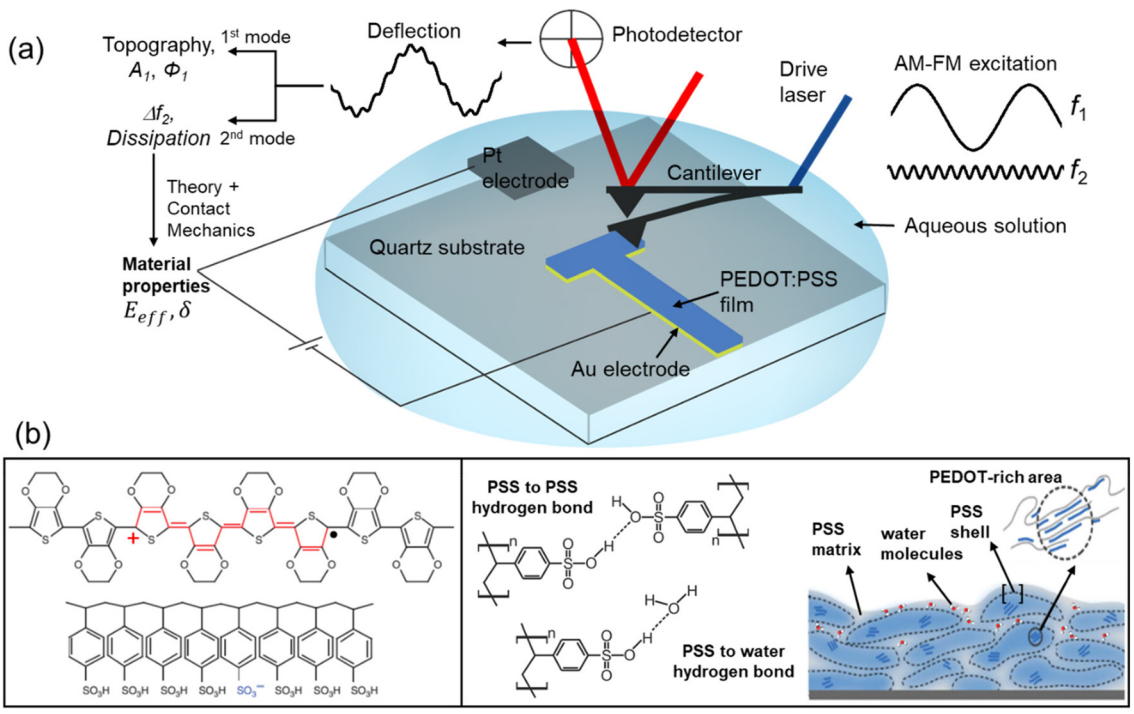

Fig. 1 (a) Bimodal AFM (AM–FM configuration) and electrical connections for the *in operando* nanomechanical characterization of organic semiconductors. The cantilever is simultaneously driven at the first and second resonances. An amplitude modulation feedback (AM) acts on the observables of the first mode, while a frequency modulation feedback (FM) controls the observables of the second mode. The amplitude A_1 and phase shift ϕ_1 of the first mode and the frequency shift Δf_2 of the second mode are used to determine the nanomechanical properties of the sample. An electrical set-up was directly implemented into the cantilever holder. It allowed external voltages to be applied between a Pt electrode and Au electrode simultaneously with bimodal AFM operation. (b) Scheme of the molecular structure of PEDOT and PSS and morphological model of a PEDOT:PSS film. Adapted and reproduced under terms of the CC-BY license.[4] Copyright 2016, Springer Nature.

grains reveal compositional variations. The Young's modulus map (Fig. 2c) is highly correlated with the energy dissipation map. There, the central region of the grains gives a lower Young's modulus value (2–3 GPa) than the narrow strip surrounding the grains (~6 GPa).

The nanomechanical maps appear consistent with the PEDOT:PSS model illustrated in Fig. 1b. In this model, the PEDOT:PSS film is made from PEDOT-rich cores surrounded by shells composed of PSS chains. The core–shell system is immersed in a hydrophilic matrix made from PSS.[4,34–37,44] Thus, the strips that surround the grains are identified with the PSS matrix. The nanomechanical maps indicate that the matrix provides a rigid framework. Paradoxically, the PSS matrix is also characterized by higher energy dissipation values with respect to the central regions. We attributed this observation to the hydrophilicity of the PSS matrix. The sulfonate groups of PSS molecules might form hydrogen bonds with other sulfonate groups and with water molecules (Fig. 1b).[36,37] Therefore, those regions are prone to adsorbing water from the humid air which, in turn, favours the formation of small nano-sized menisci between the tip and the polymer surface. The formation and rupture of the water nano-meniscus are a source of energy dissipation.[45] For that reason, more dissipation is observed on the PSS matrix than on the PSS shell and PEDOT-rich areas. Force–distance curves performed on a central and a border region of the grains support the above model (ESI Fig. S3†).

In some of the grains we observed variations across the central region. Those changes were attributed to the presence of PEDOT-rich areas, which should give rise to lower values.

Compositional variations of the PEDOT and PSS regions at the surface of the polymer film were confirmed by high-resolution AFM. Using a multifrequency AFM approach based on the excitation of the cantilever with small amplitudes at its second mode,[46,47] we obtained molecular resolution images of PSS and PEDOT lamellae (ESI Fig. S6†). These images revealed two different lamellar structures characterized, respectively, by 0.79 nm and 1.25 nm characteristic length scales. The smaller periodicity described the ordering of PSS chains while the larger was attributed to lamellar structures formed by PEDOT molecules.[48]

Nanomechanical maps of PEDOT:PSS in aqueous solutions

The topographic maps of PEDOT:PSS thin films (Fig. 3a and b) obtained in air and in an aqueous solution both revealed a granular morphology. The grain diameter (average value) was significantly larger in water: it increased from 38.2 ± 9.1 nm (dry) to 75.8 ± 15.2 nm (aqueous solution). The organic semiconductor thickness also showed an increase from 185 nm (dry (RH = 23%)) to 254 nm in the wet state (immersed in the solution). The thickness was measured with respect to the surface of the gold electrode (mean thickness equals 65 nm). The above observation is in agreement with previous measurements.[49] The Young's modulus maps (bottom panels in Fig. 3a and b) acquired simultaneously with the topography preserved the features of the topography. The average value of the modulus decreased from 2.9 ± 1.8 (dry) to 0.5 ± 0.2 GPa (aqueous). Previous measurements performed on electrochemically deposited PEDOT thin films in air provided a modulus value of 2.6 ± 1.4 GPa.[50] This value is close to the ones reported here for the PEDOT regions (2–4 GPa).

The above results underline the role of the PSS matrix in controlling the nanomechanical properties. The PSS regions are hygroscopic. Upon immersion in water, they adsorb water. Water adsorption weakens the inter PSS–PSS hydrogen bonds. This process leads to (i) the swelling of the film, (ii) the increase of the grain diameter, and (iii) the decrease of the Young's modulus.

In operando nanomechanical mapping of PEDOT:PSS in aqueous solutions

The electrical and optical properties of PEDOT:PSS thin films can be controlled by the application of a voltage bias in an aqueous electrolyte solution.[4,19,20] The driving of cations in the film, induced by charge balance, reduces the density of

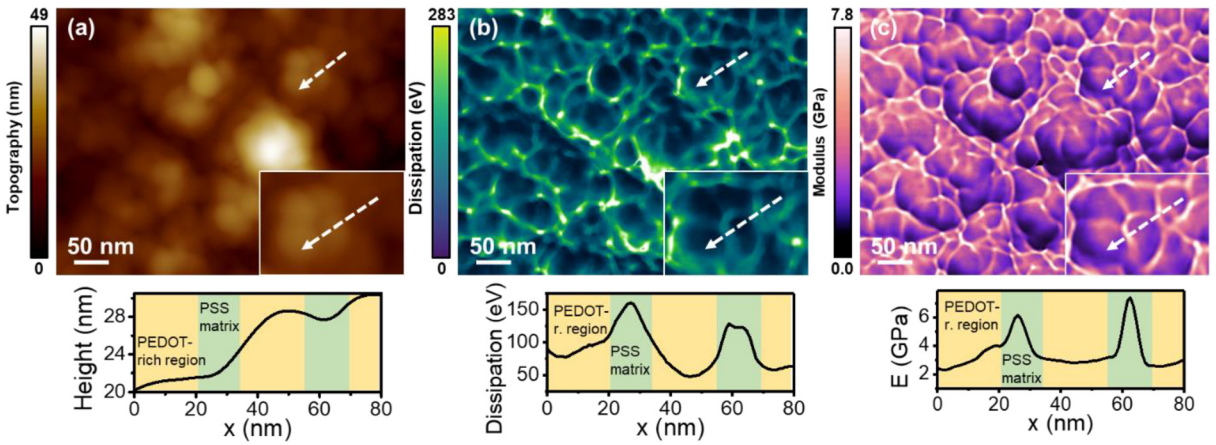

Fig. 2 (a) Topography map. (b) Energy dissipation map. (c) Young's modulus map. The above maps were obtained simultaneously in air (RH = 23%). The panels at the bottom show the cross-sections along the lines marked in the maps. Information regarding the bimodal AFM parameters is given in Table S1.† The number of pixels was 512 × 393 and the fast scanning frequency was 4.9 Hz.

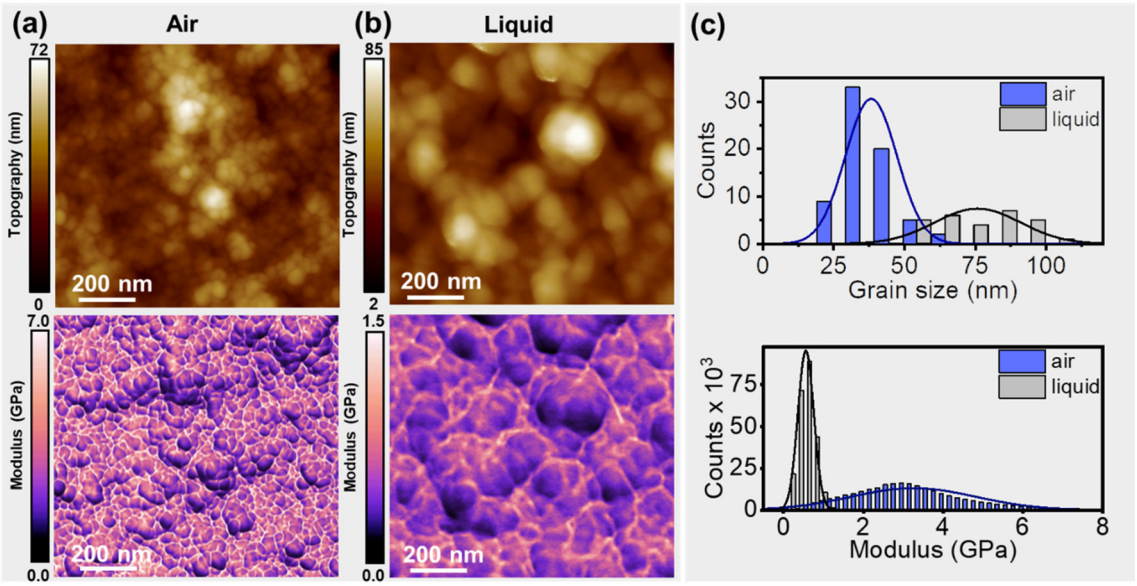

Fig. 3 (a) Topography (top) and Young's modulus map of a PEDOT:PSS film obtained in air (RH = 23%). (b) Topography (top) and Young's modulus map of a PEDOT:PSS film immersed in a KCl solution (50 mM). (c) Histogram and Gaussian fit of the grain diameter and the Young's modulus. The values were obtained from panels (a) and (b). The average grain diameter in air is about 39 nm while in liquid it is about 76 nm. The Young's modulus (average) value is 2.9 GPa (dry) and 0.5 GPa (in solution). Information regarding the bimodal AFM parameters is given in Table S1.† The number of pixels was 512 × 470; the fast-scanning frequency was 3.3 Hz (a) and 1.95 Hz (b).

mobile holes, and thus, effectively, de-dopes the organic semiconductor (see the ESI Fig. S4†).[19] We hypothesized that the nanomechanical properties should also be influenced by the bias voltage.

To demonstrate the effect of the ion uptake on the nanomechanical properties, we performed the measurements simultaneously with the application of the bias voltage. We modified the standard bimodal AFM probe holder by introducing two electrode leads (see the ESI†), one (Pt electrode) controlling the electrolyte and the other (Au electrode) coated with PEDOT:PSS. In the new set-up, the electrodes, cantilever, and PEDOT:PSS film were fully immersed in the solution. Specifically, we generated nanomechanical maps at $\Delta V = 0$ V (doped state) and $\Delta V = 0.8$ V (de-doped state). The voltage bias was applied between the Pt electrode and a gold/PEDOT:PSS electrode (Fig. 4a).

Bimodal AFM was performed on a region that included the PEDOT:PSS film and the quartz substrate. Neither the structural nor the mechanical properties of the quartz substrate were affected by the application of a bias. Therefore, we chose the elastic modulus measured on the quartz as a reference to calibrate the Young's modulus of the thin film (see the Experimental section). This approach prevented undesirable changes in the tip's geometry affecting the interpretation of the nanomechanical measurements on the film.

Two main features were observed by applying a positive bias of 0.8 V, *viz.*, a reduction of the Young's modulus and the swelling of the film. We discuss those effects separately.

Fig. 5 shows height cross-sections across the quartz substrate–gold/PEDOT:PSS interface. We have also included a cross-section from the quartz–gold interface as a reference. The cross-sections quantified the increase in the film thickness by immersion in the solution. More importantly, we noted a further increase in the thickness by applying a de-doping voltage of 0.8 V.

We can compare the observed swelling at 0.8 V (Δh = 73 nm) with an estimation of the number of cations of the solution incorporated into the film using a 1D version of Malliaras and co-workers' model.[51] This model considered that the mean distance between cations equals 1.8 nm. For a PEDOT:PSS film of 185 nm thickness (dry state, RH = 23%), on average there should be about 103 sites available for K^+ uptake in the vertical direction. At 0.8 V, all the PSS sites should bear hydrated K^+ ions. By assuming that K^+ ions carry inside the organic layer 4 water molecules (the first hydration shell), the diameter of the K^+–H_2O system should be about 0.66 nm.[52] Those assumptions give an increase in thickness of $\Delta h \approx$ 68 nm. The above value compares well with the difference observed between h (wet (0.8 V)) and h (dry), Δh = 73 nm. In short, the *in operando* bimodal data are in agreement with previous macroscopic observations that related the film swelling to ion uptake.[21] Furthermore, they link quantitatively the observed swelling with the number of cations.

To provide a more comprehensive understanding of the nanomechanical properties of PEDOT:PSS films, we performed bimodal AFM measurements while switching back and forth the bias from doping to de-doping states. The experimental run took about 80 minutes. Fig. 6a shows the relative change in the Young's modulus (black circles) as a function of the bias from doping (0 V) to de-doping (0.8 V) voltage. The

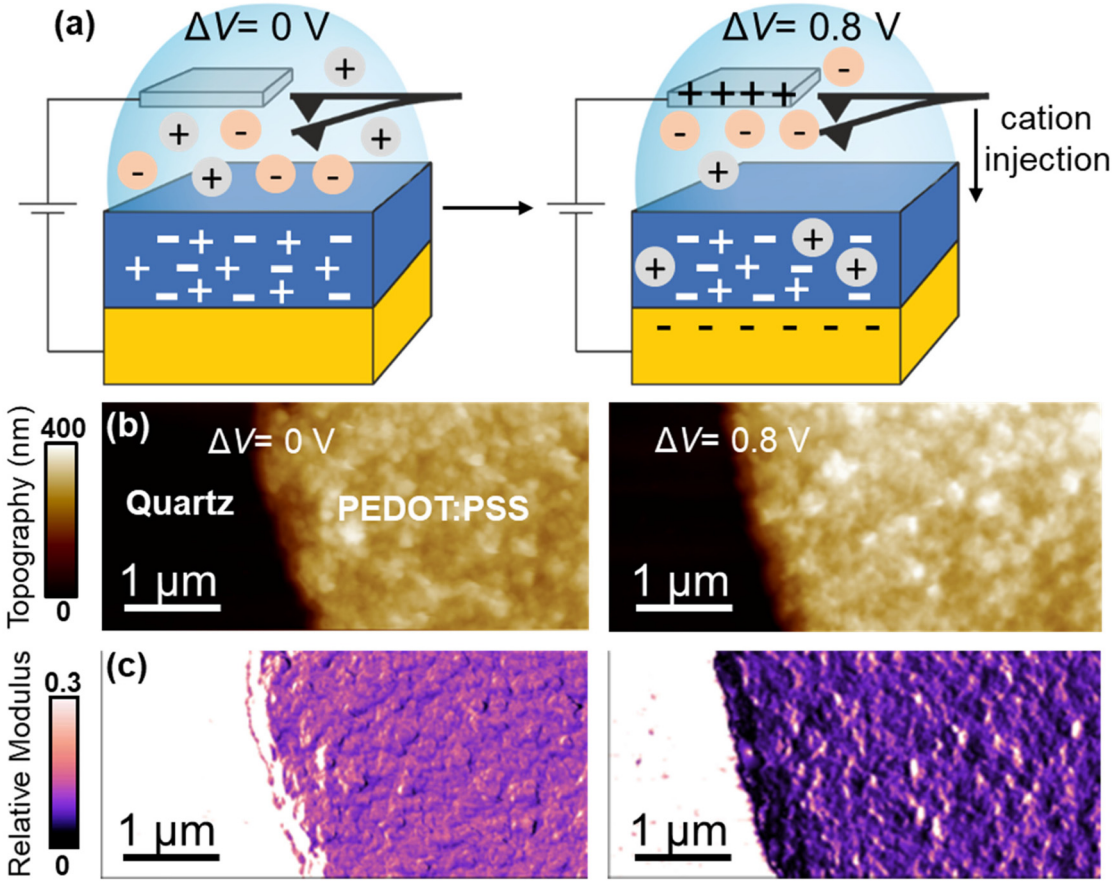

Fig. 4 (a) Scheme of the *in operando* bimodal AFM experiments. The PEDOT:PSS film is immersed in 50 mM KCl solution. Doping (0 V) and de-doping (0.8 V) conditions are illustrated. (b) Topography. (c) Young's modulus maps. Topography and Young's modulus maps, either doping or de-doping voltages, were acquired simultaneously. Information regarding the bimodal AFM parameters is given in Table S1.† The number of pixels was 512 × 256 and the fast scanning frequency was 2.8 Hz.

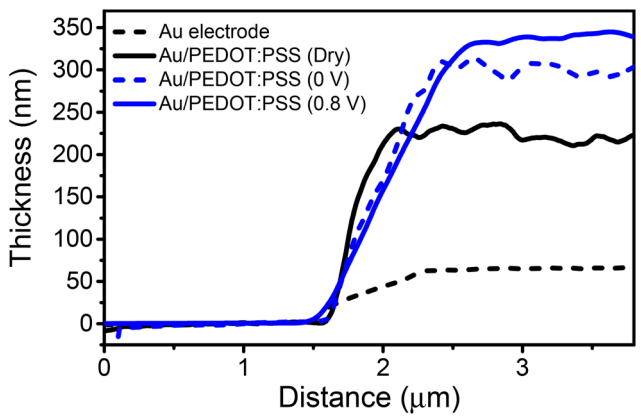

Fig. 5 Variation of the thickness as a function of the doping/de-doping voltages. The quartz substrate is the reference baseline. The thickness first increases by immersion in the solution. A further increase is observed under de-doping (cation injection) conditions.

de-doping voltage was chosen to facilitate cation uptake while preventing water hydrolysis. The relative modulus was defined as $\Delta E = (E(t) - E_0)/E_0$ where E_0 is the Young's modulus of the wet film at $t = 0$ s and $\Delta V = 0$ V. The Young's modulus decayed with the sequence of voltages towards a saturation value that amounted to about a 70% reduction. After the first two cycles, the elastic modulus decreased at the de-doping bias (*i.e.* for cations driven into the film) while it increased in the doped state, with variations of about 10%.

Fig. 6b shows the distribution of the normalized modulus in the wet condition for a bias of 0 V and for a positive bias of 0.8 V. The elastic modulus distributions were measured at the end of the sequence shown in Fig. 6a. By de-doping the film, the maximum of the distribution was shifted to lower Young's modulus values. We observed a reduction of the Young's modulus of about 70% at the end of the experimental run.

In a similar but different PEDOT:PSS sample, we repeated the nanomechanical measurements in the doped state ($\Delta V = 0$ V). Consecutive nanomechanical maps were acquired during 80 min. The results (blue dots in Fig. 6a) showed that the Young's modulus remained constant (within the experimental error). We also performed additional experiments by reversing the polarity ($\Delta V = -0.5$ V). In this case, the Young's modulus remained practically constant during the sequence of voltage pulses (Fig. 6c). A small increase in the Young's modulus of

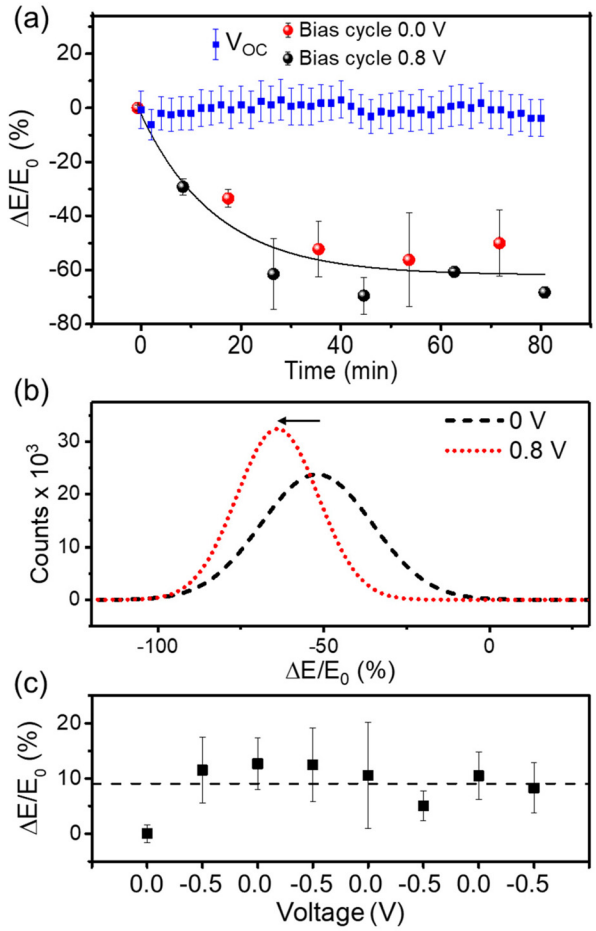

Fig. 6 (a) Variation of the Young's modulus after switching back and forward between doping (0 V, red dots) and de-doping (0.8 V, black dots) states. The squares in blue refer to the Young's modulus at the open circuit value. (b) Young's modulus shift of PEDOT:PSS film immersed in 50 mM KCl solution at doping and de-doping states. Young's modulus distributions are obtained from maps as the ones shown in Fig. 4. (c) Variation of Young's modulus between 0 V and a negative bias (−0.5 V). The relative variation of Young's modulus is defined as $\Delta E = (E(t) - E_0)$ where E_0 is the Young's modulus at $t = 0$ and $\Delta V = 0$; $E(t)$ is Young's modulus at a given time t.

about 10% was observed after the application of the first −0.5 V sequence. Negative voltages should prevent the uptake of cations by the film, which is confirmed by the nanomechanical data. The minor increase in the modulus might indicate the existence of an electrical field-induced strain.

The application of a positive voltage to the Pt electrode drives the anions Cl^- towards Pt and the cations K^+ into the PEDOT:PSS film. Cations are combined with sulfonate anions of the PEDOT:PSS, which leads to the de-doping of the channel of the device. The bimodal AFM data show that the initial modulus is not restored when cations are driven out from the film ($\Delta V = 0$ V). This observation is consistent with previous observations of PEDOT:PSS organic electronic devices that showed that a few de-doping/re-doping cycles were required to reach a reproducible and stable current behaviour. This was attributed to the formation of percolation channels due to cation injection, which generates a persistent hydration of the polymer film.[19] The nanomechanical data show that the persistent hydration introduces a non-reversible change in the mechanical properties. The non-reversible behaviour of PEDOT:PSS swelling upon ion insertion was previously explained by the presence of a bulky hydrophilic PSS phase acting as a site for the accumulation of ions not involved in the de-doping process.[21]

Conclusion

We performed a comprehensive characterization of the nanomechanical properties and structure of PEDOT:PSS films. The nanomechanical maps revealed a granular structure made from PEDOT:PSS grains embedded in a PSS matrix. Within the grains, we observed the lamellar structure of PEDOT-rich areas. Furthermore, we resolved the molecular structure of PSS regions.

In operando bimodal AFM revealed how the ion uptake modified both the structure and the nanomechanical response of a PEDOT:PSS film. The immersion of the film in an aqueous solution followed by the application of a doping/de-doping voltage sequence produced a decay of the modulus film as a function of time. The softening was associated with a persistent change in the hydration structure of the film promoted by the cations. Additionally, from our data it is evident that the injection/removal of cations allows for a softening/stiffening of the polymer film.

It was previously established that the uptake of cations in PEDOT:PSS devices modifies their electronic and optical properties. Bimodal AFM demonstrated that this process introduced a non-reversible softening of the film. Modulating this effect will enhance the *in vivo* application of PEDOT:PSS devices.[53]

Experimental

Materials

EDOT (ethylenedioxythiophene) and Na^+PSS^- (sodium poly (sterene-sulfonate)) were purchased from Sigma-Aldrich. Test patterns made from gold electrodes on a quartz substrate were purchased by Fondazione Bruno Kessler (Italy). Aqueous solutions of 50 mM KCl were prepared by dissolving KCl (≥99%, Sigma-Aldrich) in ultra-pure water.

Device preparation

PEDOT:PSS thin films were prepared by means of electrodeposition on gold electrodes. Some microliters of a solution of EDOT (0.01 M) containing an excess of Na^+PSS^- (0.8%, w/w) were deposited over the test pattern. A constant current (1 μA) was applied between the two terminals of the device for a total time of 10 s. The thickness of the film (185 ± 7 nm) was measured through AFM. Since the purpose of the study was to

characterize the mechanical properties of PEDOT:PSS, the use of 185 nm-thick films avoided the application of bottom-effect corrections.[54]

Bimodal AFM

The Young's modulus was obtained by applying the theoretical framework developed previously.[30,31,41] This framework is based on Hertz contact mechanics. Bimodal AFM is implemented using the software of a Cypher S (Asylum Research, Oxford Instruments, CA, USA). Measurements were performed in air (RH = 23%) and in electrolyte solutions (50 mM KCl). Photothermal excitation was applied to drive the oscillation of the cantilever. The acquisition time was 2–3 minutes for each image. *In operando* bimodal AFM was accomplished by applying a voltage between the Pt and Au electrodes. We used PPP-NCH-AuD and PPP-NCST-AuD (NanoAndMore, Germany) and HQ-150-AuD (Asylum Research, Oxford Instruments, CA, USA) cantilevers. The force constant of the first mode of the PPP-NCH-AuD cantilevers was calibrated using the multiple reference calibration method.[55] The force constants of the first mode of HQ-150-AuD and PPP-NCST-AuD cantilevers were calibrated by taking a force–distance curve on a Si sample. For all cantilevers, the force constant of the second mode was calibrated using the force constant–frequency power law relationship.[56] The radii of the tips used in Fig. 2 and 3 were calibrated using a test sample with a well-characterized Young's modulus (polystyrene, with E = 2.7 GPa). The Poisson coefficient of PEDOT:PSS was assumed to be 0.35.[37] Calibration values and bimodal parameters are given in Table S1 of the ESI.† The radii of the tips used in Fig. 4 and 6 were calibrated as follows: the tip radius was changed to keep the Young's modulus of the quartz constant, considering the Young's modulus of the quartz independent of the applied voltage. Thus, the change in PEDOT:PSS elastic modulus was normalized to that of the quartz.

A custom-built electrical set-up (Fig. S4†) was incorporated into the AFM holder of a Cypher S (Asylum Research, Oxford Instruments, CA, USA). It consisted of a thin platinum electrode placed in the vicinity of the cantilever. A cable connects the Pt electrode to the electrical source measure unit (SMU, Keithley 4200). Biases were applied between the Pt electrode and the gold electrode below the PEDOT:PSS film. The gold electrode was contacted to the wire of the power supplier using silver paint. Two biases (ΔV = 0 and 0.8 V) were applied for 120 s before starting the bimodal AFM measurements. The film was considered to be fully penetrated by cations after 120 s (K^+ mobility = 2.2×10^3 cm^2 V^{-1} s^{-1}).[4,19]

Amplitude modulation AFM

Extensive characterization of the PEDOT:PSS films prior to the bimodal AFM mapping was performed with an NX20 AFM (Park systems, South Korea) and a Cypher S (Asylum Research, Oxford Instruments, CA, USA). The images were obtained in the amplitude modulation configuration.[57] The molecular resolution images (Fig. S6†) were also acquired in the AM mode. In this case, very small oscillation amplitudes (0.1–0.5 nm) were applied to the cantilever. The small amplitude operation enhances the sensitivity to short-range interaction forces and as a consequence allows a high spatial resolution to be obtained.[58] Experiments were performed in air (RH = 23%) using PPP-NCH-AuD cantilevers (NanoAndMore, Germany) driven in their second flexural mode. Typical values were f_2 = 1800 kHz, k_2 = 2000 N m^{-1} and Q_2 = 600.

Author contributions

S. B. performed the experiments. S. B. and S. D. prepared the samples, designed and assembled the electrical set-up. S. B. and R. G. designed and analysed the experiments with contributions from F. B. and S. D. S. B. and R. G. wrote the manuscript and the ESI† with contributions from F. B. and S. D. All the authors discussed the results.

Conflicts of interest

There are no conflicts of interest to declare.

Acknowledgements

We acknowledge the funding support of the European Commission Marie Sklodowska-Curie grant agreement no. 721874 SPM 2.0. RG acknowledges funding the Ministerio de Ciencia, Innovación y Universidades (PID2019-106801GB-I00) and CSIC (202050E013). FB acknowledges IIT and UNIMORE for support.

References

1 Z. Bao, J. A. Rogers and H. E. Katz, *J. Mater. Chem.*, 1999, **9**, 1895–1904.
2 T. Someya, Z. Bao and G. G. Malliaras, *Nature*, 2016, **540**, 379–385.
3 R. Wu, M. Matta, B. D. Paulsen and J. Rivnay, *Chem. Rev.*, 2022, **122**, 4493–4551.
4 J. Rivnay, S. Inal, B. A. Collins, M. Sessolo, E. Stavrinidou, X. Strakosas, C. Tassone, D. M. Delongchamp and G. G. Malliaras, *Nat. Commun.*, 2016, **7**, 11287.
5 M. Moser, J. Gladisch, S. Ghosh, T. C. Hidalgo, J. F. Ponder, R. Sheelamanthula, Q. Thiburce, N. Gasparini, A. Wadsworth, A. Salleo, S. Inal, M. Berggren, I. Zozoulenko, E. Stavrinidou and I. McCulloch, *Adv. Funct. Mater.*, 2021, **31**, 1–10.
6 S. Casalini, A. C. Dumitru, F. Leonardi, C. A. Bortolotti, E. T. Herruzo, A. Campana, R. F. de Oliveira, T. Cramer, R. Garcia and F. Biscarini, *ACS Nano*, 2015, **9**, 5051–5062.
7 A. Kyndiah, M. Checa, F. Leonardi, R. Millan-Solsona, M. Di Muzio, S. Tanwar, L. Fumagalli, M. Mas-Torrent and G. Gomila, *Adv. Funct. Mater.*, 2021, **31**, 2008032.

8 S. Inal, J. Rivnay, A. O. Suiu, G. G. Malliaras and I. McCulloch, *Acc. Chem. Res.*, 2018, **51**, 1368–1376.
9 D. Khodagholy, T. Doublet, M. Gurfinkel, P. Quilichini, E. Ismailova, P. Leleux, T. Herve, S. Sanaur, C. Bernard and G. G. Malliaras, *Adv. Mater.*, 2011, **23**, 268–272.
10 C. Diacci, J. W. Lee, P. Janson, G. Dufil, G. Méhes, M. Berggren, D. T. Simon and E. Stavrinidou, *Adv. Mater. Technol.*, 2020, **5**, 1900262.
11 M. Giordani, M. Sensi, M. Berto, M. Di Lauro, C. A. Bortolotti, H. L. Gomes, M. Zoli, F. Zerbetto, L. Fadiga and F. Biscarini, *Adv. Funct. Mater.*, 2020, **30**, 2002141.
12 D. Khodagholy, J. N. Gelinas, T. Thesen, W. Doyle, O. Devinsky, G. G. Malliaras and G. Buzsáki, *Nat. Neurosci.*, 2015, **18**, 310–315.
13 A. Campana, T. Cramer, D. T. Simon, M. Berggren and F. Biscarini, *Adv. Mater.*, 2014, **26**, 3874–3878.
14 F. Amorini, I. Zironi, M. Marzocchi, I. Gualandi, M. Calienni, T. Cramer, B. Fraboni and G. Castellani, *ACS Appl. Mater. Interfaces*, 2017, **9**, 6679–6689.
15 S. E. Root, S. Savagatrup, A. D. Printz, D. Rodriquez and D. J. Lipomi, *Chem. Rev.*, 2017, **117**, 6467–6499.
16 L. V. Kayser and D. J. Lipomi, *Adv. Mater.*, 2019, **31**, 1–13.
17 U. Lang, N. Naujoks and J. Dual, *Synth. Met.*, 2009, **159**, 473–479.
18 M. ElMahmoudy, S. Inal, A. Charrier, I. Uguz, G. G. Malliaras and S. Sanaur, *Macromol. Mater. Eng.*, 2017, **302**, 1–8.
19 E. Stavrinidou, P. Leleux, H. Rajaona, D. Khodagholy, J. Rivnay, M. Lindau, S. Sanaur and G. G. Malliaras, *Adv. Mater.*, 2013, **25**, 4488–4493.
20 S. Inal, G. G. Malliaras and J. Rivnay, *J. Mater. Chem. C*, 2016, **4**, 3942–3947.
21 A. Savva, S. Wustoni and S. Inal, *J. Mater. Chem. C*, 2018, **6**, 12023–12030.
22 R. Giridharagopal, L. Q. Flagg, J. S. Harrison, M. E. Ziffer, J. Onorato, C. K. Luscombe and D. S. Ginger, *Nat. Mater.*, 2017, **16**, 1–6.
23 C. G. Bischak, L. Q. Flagg, K. Yan, T. Rehman, D. W. Davies, R. J. Quezada, J. W. Onorato, C. K. Luscombe, Y. Diao, C. Z. Li and D. S. Ginger, *J. Am. Chem. Soc.*, 2020, **142**, 7434–7442.
24 A. Kyndiah, M. Checa, F. Leonardi, R. Millan-Solsona, M. Di Muzio, S. Tanwar, L. Fumagalli, M. Mas-Torrent and G. Gomila, *Adv. Funct. Mater.*, 2020, 2008032.
25 A. Liscio, V. Palermo and P. Samorì, *Acc. Chem. Res.*, 2010, **43**, 541–550.
26 R. Garcia, *Chem. Soc. Rev.*, 2020, **49**, 5850–5884.
27 M. E. Dokukin and I. Sokolov, *Sci. Rep.*, 2017, **7**, 11828.
28 G. Stan and S. W. King, *J. Vac. Sci. Technol., B: Nanotechnol. Microelectron.: Mater., Process., Meas., Phenom.*, 2020, **38**, 060801.
29 H. Huang, I. Dobryden, P.-A. Thorén, L. Ejenstam, J. Pan, M. L. Fielden, D. B. Haviland and P. M. Claesson, *Compos. Sci. Technol.*, 2017, **150**, 111–119.
30 C. A. Amo, A. P. Perrino, A. F. Payam and R. Garcia, *ACS Nano*, 2017, **11**, 8650–8659.
31 S. Benaglia, V. G. Gisbert, A. P. Perrino, C. A. Amo and R. Garcia, *Nat. Protoc.*, 2018, **13**, 2890–2907.
32 V. G. Gisbert, S. Benaglia, M. R. Uhlig, R. Proksch and R. Garcia, *ACS Nano*, 2021, **15**, 1850–1857.
33 D. Ebeling and S. D. Solares, *Nanotechnology*, 2013, **24**, 135702.
34 A. V. Volkov, K. Wijeratne, E. Mitraka, U. Ail, D. Zhao, K. Tybrandt, J. W. Andreasen, M. Berggren, X. Crispin and I. V. Zozoulenko, *Adv. Funct. Mater.*, 2017, **27**, 1–10.
35 A. M. Nardes, R. A. J. Janssen and M. Kemerink, *Adv. Funct. Mater.*, 2008, **18**, 865–871.
36 J. Zhou, D. H. Anjum, L. Chen, X. Xu, I. A. Ventura, L. Jiang and G. Lubineau, *J. Mater. Chem. C*, 2014, **2**, 9903–9910.
37 U. Lang, E. Müller, N. Naujoks and J. Dual, *Adv. Funct. Mater.*, 2009, **19**, 1215–1220.
38 T. R. Rodriguez and R. Garcia, *Appl. Phys. Lett.*, 2004, **84**, 449–451.
39 G. Chawla and S. D. Solares, *Appl. Phys. Lett.*, 2011, **99**, 074103.
40 A. Labuda, M. Kocun, W. Meinhold, D. Walters and R. Proksch, *Beilstein J. Nanotechnol.*, 2016, **7**, 970–982.
41 S. Benaglia, C. A. Amo and R. Garcia, *Nanoscale*, 2019, **11**, 15289–15297.
42 E. T. Herruzo, A. P. Perrino and R. Garcia, *Nat. Commun.*, 2014, **5**, 3126.
43 R. Garcia, C. J. Gómez, N. F. Martinez, S. Patil, C. Dietz and R. Magerle, *Phys. Rev. Lett.*, 2006, **97**, 1–4.
44 A. M. Nardes, M. Kemerink, R. A. J. Janssen, J. A. M. Bastiaansen, N. M. M. Kiggen, B. M. W. Langeveld, A. J. J. M. Van Breemen and M. M. De Kok, *Adv. Mater.*, 2007, **19**, 1196–1200.
45 V. Barcons, A. Verdaguer, J. Font, M. Chiesa and S. Santos, *J. Phys. Chem. C*, 2012, **116**, 7757–7766.
46 T. Fukuma, K. Kobayashi, K. Matsushige and H. Yamada, *Appl. Phys. Lett.*, 2005, **87**, 034101.
47 V. V. Korolkov, A. Summerfield, A. Murphy, D. B. Amabilino, K. Watanabe, T. Taniguchi and P. H. Beton, *Nat. Commun.*, 2019, **10**, 1–8.
48 E. Hosseini, V. Ozhukil Kollath and K. Karan, *J. Mater. Chem. C*, 2020, **8**, 3982–3990.
49 M. Modarresi, A. Mehandzhiyski, M. Fahlman, K. Tybrandt and I. Zozoulenko, *Macromolecules*, 2020, **53**, 6267–6278.
50 J. Qu, L. Ouyang, C. Kuo and D. C. Martin, *Acta Biomater.*, 2016, **31**, 114–121.
51 C. M. Proctor, J. Rivnay and G. G. Malliaras, *J. Polym. Sci., Part B: Polym. Phys.*, 2016, **54**, 1433–1436.
52 I. U. Vakarelski, K. Ishimura and K. Higashitani, *J. Colloid Interface Sci.*, 2000, **227**, 111–118.
53 M. Di Lauro, E. Zucchini, A. De Salvo, E. Delfino, M. Bianchi, M. Murgia, S. Carli, F. Biscarini and L. Fadiga, *Adv. Mater. Interfaces*, 2022, 2101798.
54 V. G. Gisbert and R. Garcia, *ACS Nano*, 2021, **15**, 20574–20581.
55 J. E. Sader and J. R. Friend, *Rev. Sci. Instrum.*, 2015, **86**, 2014–2016.

56 A. Labuda, M. Kocun, M. Lysy, T. Walsh, J. Meinhold, T. Proksch, W. Meinhold, C. Anderson and R. Proksch, *Rev. Sci. Instrum.*, 2016, **87**, 073705.
57 R. Garcia and A. San Paulo, *Phys. Rev. B: Condens. Matter Mater. Phys.*, 1999, **60**, 4961–4967.
58 C.-Y. Lai, S. Santos and M. Chiesa, *ACS Nano*, 2016, **10**, 6265–6272.